Sparse multi-nanopore osmotic power generators

Tsutsui, Makusu

Yokota, Kazumichi

Leong, Iat Wai

He, Yuhui

他

出版情報：Cell Reports Physical Science. 3 (10), pp.101065-, 2022-10. Elsevier
バージョン：

Cell Reports
Physical Science

CellPress
OPEN ACCESS

Article

Sparse multi-nanopore osmotic power generators

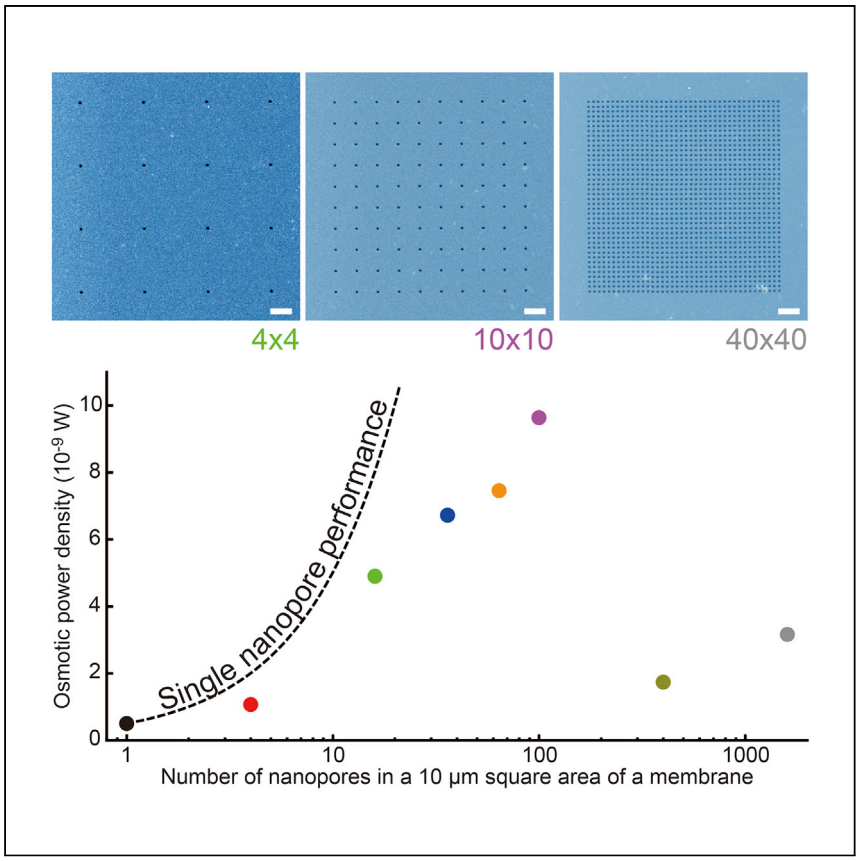

By optimizing the structures and positions of nanopores, Tsutsui et al. demonstrate that silicon nitride multi-pore membranes can become a good osmotic power generator.

Makusu Tsutsui, Kazumichi Yokota, Iat Wai Leong, Yuhui He, Tomoji Kawai

tsutsui@sanken.osaka-u.ac.jp (M.T.)
kawai@sanken.osaka-u.ac.jp (T.K.)

Highlights

Single SiN_x nanopore allows highly efficient osmotic energy conversion

Inter-nanopore interference broadens cross-membrane salt concentration distributions

Control of nanopore structures and positions can maximize the osmotic power output

Tsutsui et al., Cell Reports Physical Science 3, 101065
October 19, 2022
https://doi.org/10.1016/j.xcrp.2022.101065

Cell Reports
Physical Science

CellPress
OPEN ACCESS

Article

Sparse multi-nanopore osmotic power generators

Makusu Tsutsui,[1,4,*] Kazumichi Yokota,[2] Iat Wai Leong,[1] Yuhui He,[3] and Tomoji Kawai[1,*]

SUMMARY

Ultrathin nanopore membrane is an emerging energy harvesting system capable of generating electricity from salinity gradients. Here, we report on the evaluation of its practical feasibility by exploring the energy conversion efficiency of single to densely packed multi-pores in a thin silicon nitride. The ionic current characteristics of single pores reveal a quasi-perfect cation selectivity when shrinking the diameter to 20 nm. The perm-selective nanopore is shown to yield osmotic power of 160 pW under a 1,000-fold transmembrane salt concentration difference. Meanwhile, whereas larger energy is gained by parallelly integrating multiple pores, excessive porosity also led to degraded energy conversion efficiency, thereby demonstrating an optimal power density of 100 W per square meter for 100 nm-sized multi-nanopores with a grid spacing of 1 μm. The present findings offer a guide to design highly efficient nanopore membrane osmotic power generators.

INTRODUCTION

Non-uniform salinity conditions at two ends of a conduit in a membrane induce directional ion flow via diffusion. This phenomenon has been considered a promising route for renewable energy that allows us to convert Gibbs free energy into electricity through leveraging perm selectivity of functional porous membranes.[1–4] Its essential mechanism lies in the idea of prohibiting the flow of cations or anions via the electrostatic repulsion at the channel wall so as to induce electric potential difference upon ion migration.[5–7] The nanoscopic size of the fluid paths is thus of central importance to have a substantial influence of the electric field for highly selective transport, or otherwise little osmotic energy can be generated due to the non-selective ion flow in the large space under the spatially restricted surface charge effects by screening in the electrolyte media.[3]

Besides the ion selectivity, enhanced ionic conductance is required for gaining a high energy conversion efficiency, which is often a key challenge when employing extremely high length-to-diameter aspect ratio nanochannels in self-organized porous membranes.[8–10] In this regard, it is noticeable that the high conductance of a relatively large disk-like nanopore in two-dimensional (2D) materials such as graphene[11] and MoS_2[12] is reported to enable giant osmotic power densities amounting to sub-MW/m^2.[12,13] Despite the huge potential, however, little efforts have been devoted to elucidate the physics underlying the exceptional ion selectivity of the low aspect ratio pores and evaluate the practical usefulness when integrated in a form of densely packed nanopore membranes,[14] where ion concentration polarization[15] as well as inter-pore electric field interference[16] may affect the overall performance as an osmotic power generator. To shed light on these issues, we herein investigated the salinity-gradient-driven ion transport in a single nanopore to multi-pores by leveraging the nanoscale fabrication precision of electron beam lithography to form channels of well-defined size and positions.[17]

[1]The Institute of Scientific and Industrial Research, Osaka University, 8-1 Mihogaoka, Ibaraki, Osaka 5267-0047, Japan

[2]National Institute of Advanced Industrial Science and Technology, Takamatsu, Kagawa 761-0395, Japan

[3]Wuhan National Laboratory for Optoelectronics, School of Integrated Circuits, Huazhong University of Science and Technology, Wuhan 430000, China

[4]Lead contact

*Correspondence: tsutsui@sanken.osaka-u.ac.jp (M.T.), kawai@sanken.osaka-u.ac.jp (T.K.)

https://doi.org/10.1016/j.xcrp.2022.101065

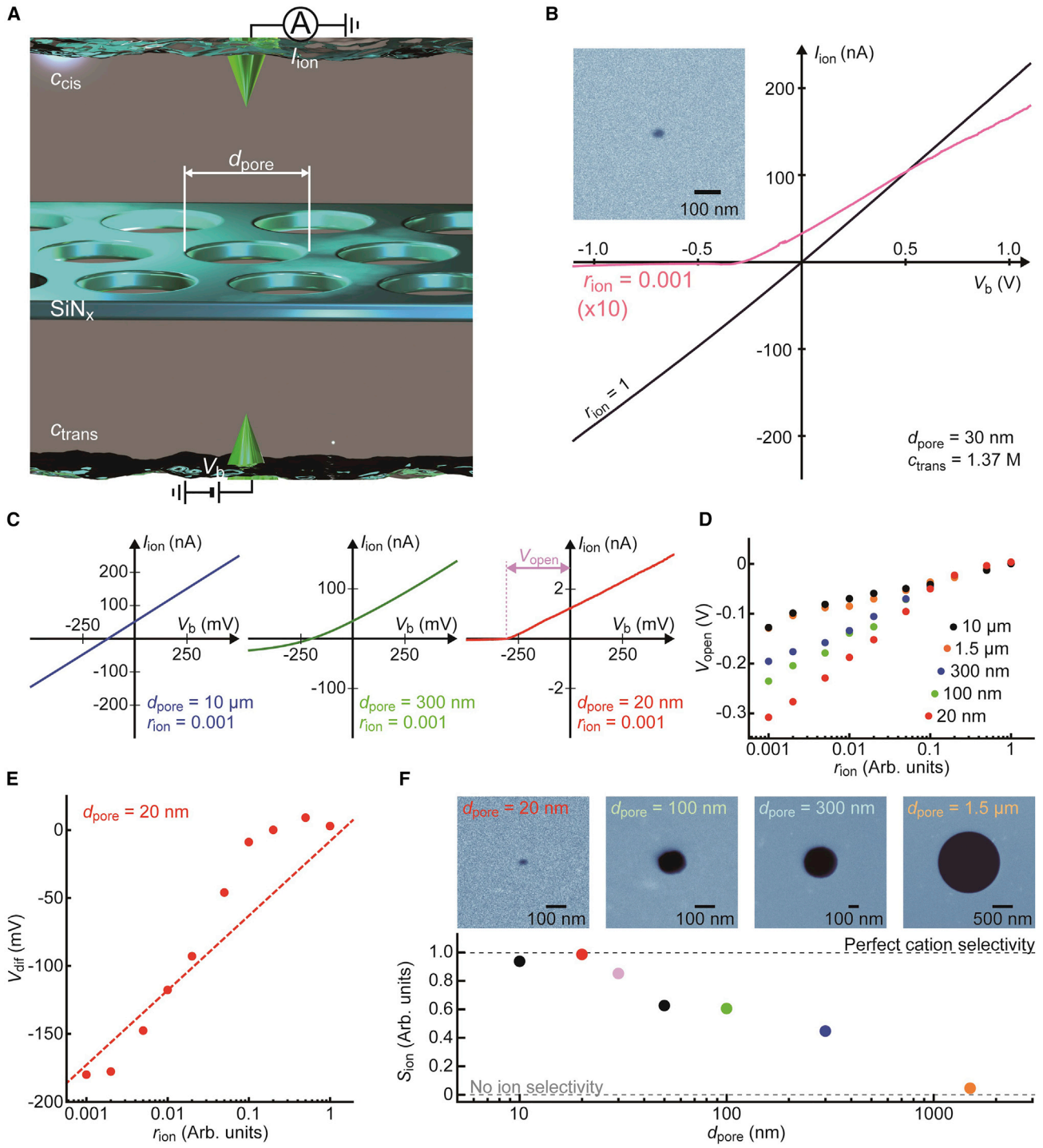

Figure 1. Ion selectivity in solid-state pores

(A) A schematic model showing the measurement of ionic current I_{ion} through nanopores of diameter d_{pore} in a 40 nm-thick SiN_x membrane under the applied voltage V_b. c_{cis} and c_{trans} denote the NaCl concentrations at *cis* and *trans*, respectively.

(B) $I_{ion} - V_b$ curves recorded in a 30 nm-sized single nanopore with (black) and without (pink) salinity gradients (denoted by the ratio $r_{ion} = c_{cis}/c_{trans}$). Inset is a scanning electron micrograph of the nanopore used.

(C) $I_{ion} - V_b$ characteristics of 10 µm- (left), 300 nm- (middle), and 20 nm-sized pores (right) under r_{ion} = 0.001. V_{open} is the open-circuit voltage.

(D) Scatterplots of V_{open} as a function of r_{ion} for pores of diameters 10 µm (black), 1.5 µm (orange), 300 nm (blue), 100 nm (green), and 20 nm (red).

Figure 1. *Continued*
(E) The diffusion-induced voltage V_{dif} plotted against r_{ion} for the 20 nm-sized nanopore. Dashed line is a logarithmic fit to the plots.
(F) Pore-size dependence of the ion selectivity factor S_{ion}. Gray and black dashed lines point to S_{ion} = 0 and 1 that represent the null and perfect cation selectivity in the fluidic channels. Insets are scanning electron microscopy images of the SiN_x pores of various diameters.

RESULTS

Ion selectivity in single nanopores

The fluidic system is comprised of two chambers connected via a hole of diameter d_{pore} in a 40 nm-thick SiN_x membrane on a Si wafer (Figures 1A and S1). Applying various salinity gradients by systematically varying the NaCl concentrations of PBS (pH 7.4) at the *cis* (c_{cis}) and *trans* (c_{trans}) in a range from 1.37 M to 1.37 mM, we measured the cross-membrane ionic current I_{ion} under voltage scans from −1 to 1 V. This electrolyte buffer was utilized since the osmotic power generation systems mainly consider energy harvesting from seawater,[1–4] which is characterized as an aqueous solution of high-concentration NaCl (at pH around 7 to 8). Linear I_{ion} versus V_b curves were obtained for the pores of d_{pore} from 10 μm to 20 nm under high ionic strength with no salt concentration difference, i.e., $r_{ion} = c_{cis}/c_{trans} = 1$, with $c_{cis} = c_{trans}$ = 1.37 M (Figure 1B). The scaling of the conductance $G = I_{ion}/V_b$ with the pore size followed Maxwell's model[18–20] with a constant resistivity of the solution ρ of 0.1 Ωm (Figure S2), which manifests the negligible influence of the membrane surface charges due to the effective screening of the electrostatic field by ions (Debye screening length λ_D is about 0.3 nm in 1.37 M NaCl).[21]

In contrast, the ionic current characteristics became non-linear under large salinity gradients in small pores (Figure 1B). At the same time, we detected positive I_{ion} at zero V_b, suggesting a stronger flow of Na^+ than Cl^- from the high to low ion concentration by diffusion (Figure 1C; see also Figures S3–S11).[11] This cation-selective transport is in fact anticipated for the SiN_x membrane pores having negative native charges[22] that serve to reject Cl^- from the channel via the electrostatic repulsion.[23]

To evaluate the d_{pore} dependence of the ion selectivity, we extracted the open-circuit voltage V_{open} from the points where I_{ion} crossed zero current during the voltage sweeps (Figure 1D).[24] Here, V_{open} includes the redox potential difference V_{red} at the electrodes exposed to the solutions of distinct electrolyte concentrations.[25] Since the Ag/AgCl rods were placed more than 10 mm away from the pores, V_{red} was expected to remain the same irrespective of d_{pore}. Indeed, the micropores larger than 1.5 μm gave quite similar V_{open} within the entire r_{ion} range measured, signifying no potential difference induced by the ion transport and hence negligibly weak selectivity for $\lambda_D \ll d_{pore}$.[11] More specifically, V_{open} scaled linearly with $\log_{10} r_{ion}$ in accordance with the thermodynamic theory for the redox potential difference E_{red}.[26]

The above results in turn indicate a pronounced ion selectivity in low depth-to-diameter aspect ratio SiN_x nanopores smaller than 300 nm. Subtracting the electrode potential, therefore, we deduced the ion diffusion-derived voltage V_{dif} through $V_{dif} = V_{open} - V_{red}$. V_{dif} reflects the asymmetry in the cation and anion diffusion as $V_{dif} = S_{ion}(k_BT/e)\ln(a_{cis}/a_{trans})$,[25] where S_{ion} is the selectivity factor denoting perfect anion and cation selectivity when S_{ion} = +1 and −1, respectively, while non-selective transport with S_{ion} = 0 (the ion activities in *cis* [a_{cis}] and *trans* [a_{trans}] were approximated to be $r_{ion} = a_{cis}/a_{trans}$).[12] Deducing the selectivity factors by linear fits to the plots of V_{dif} as a function of $\ln r_{ion}$ (Figure 1E), we found a monotonic increase in the cation selectivity with decreasing d_{pore} from 1.5 μm (Figure 1F). Noticeably, S_{ion} reached 0.99 for d_{pore} = 20 nm, manifesting quasi-perfect selectivity in the 40 nm-long channel of the radius still larger than the Debye length of 8 nm for

c_{cis} = 1.37 mM.[20] The results as a whole confirmed that high aspect ratio channel structures are not a prerequisite to achieve selective ion transport, thereby corroborating the usefulness of short nanopores for efficient osmotic power generation.[13,14]

The non-negligible perm selectivity of nanopores larger than the electrostatic screening length is attributable to its low aspect ratio structure and the surface charge conditions. In the case of high aspect ratio nanochannels in a micrometer-thick membrane such as those in anodic aluminum oxides, surface charges on the wall play predominant roles on the ion selectivity.[14] In contrast, the mechanism underlying the perm selectivity in ultrathin pores was reported to be quite different, where the chemical and physical properties, such as the exterior surface charge of the nanopores,[14,27] largely contribute to the perm-selective characteristics. Although it is not straightforward to predict the ion selectivity in the low aspect ratio nanopores, the perm-selective ion transport in the 300 nm-sized nanopore observed in the present study would not be surprising considering that ion selectivity was reported for graphene nanopores larger than the Debye length, which was explained as being due in part to the diffusive transport of high concentration counterions in the vicinity of the membrane surface.[11]

Ionic current rectification in surface-engineered nanopores

Surface engineering is known as an effective way to modify the selective ion transport properties via the tuned electrostatic potential at a nanochannel wall.[28–30] To verify its feasibility in tailoring the ionic current characteristics in the low aspect ratio nanopores, we created membranes of asymmetric charge configurations by coating the SiN_x at the *cis* side with 20 nm-thick SiO_2 and ZnO layers (Figure 2A; see also Figure S12). A pristine 100 nm-sized SiN_x nanopore (surface zeta potential $\zeta = -11$ mV as measured using a zeta sizer Nano-ZS of Malvern with the Surface Zeta Potential Cell kit ZEN1020) exhibited linear $I_{ion} - V_b$ characteristics in a dilute electrolyte buffer of $c_{cis} = c_{trans} = 1.37$ mM (Figure 2B). This is an obvious result reflecting that while the ion transport is anticipated to be partially cation selective (Figure 1G), the net ion flow is not affected by the voltage polarity due to the homogeneous negative charge distribution at the SiN_x nanopore membrane surface. In contrast, the incorporation of 20 nm ZnO led to a diode-like behavior even without a salinity gradient (Figure 2B). Considering the isoelectric points of the dielectric materials,[31] the surface potential at the *cis* side (ZnO) is considered charged positive, in contrast to that at the *trans* side (SiN_x) being electrically negative (here, we note that whereas we obtained $\zeta = -1$ mV for ZnO, its value may not be accurate, as the zeta sizer used was not designed for measuring positively charged surfaces). The ion transport through such a Janus nanopore membrane is predicted to be highly asymmetric due to the electrostatic interactions of ions with the local dielectrics:[32,33] the electric force between the current-carrying ions and membrane surface is attractive, serving to draw more cations and anions into the nanopore under positive V_b; on contrary, the repulsive interactions between ZnO (SiN_x) and cations (anions) in *cis* (*trans*) impede their translocation, serving to suppress the ionic current under negative voltage through depleting the ions inside the nanopore.[32,33] Meanwhile, the nanofluidic channel demonstrated no notable rectification after the SiO_2 deposition ($\zeta = -54$ mV) since the surface potential at the entire membrane surface remains negative, bringing less significant asymmetry in the cross-membrane surface potential profile.

The dielectric coatings also affected the open-circuit voltage. While the SiN_x nanopore of 100 nm diameter showed no voltage offset at zero ionic current, the ZnO- and SiO_2-coated pores revealed negative and positive V_{open}, respectively, in a dilute

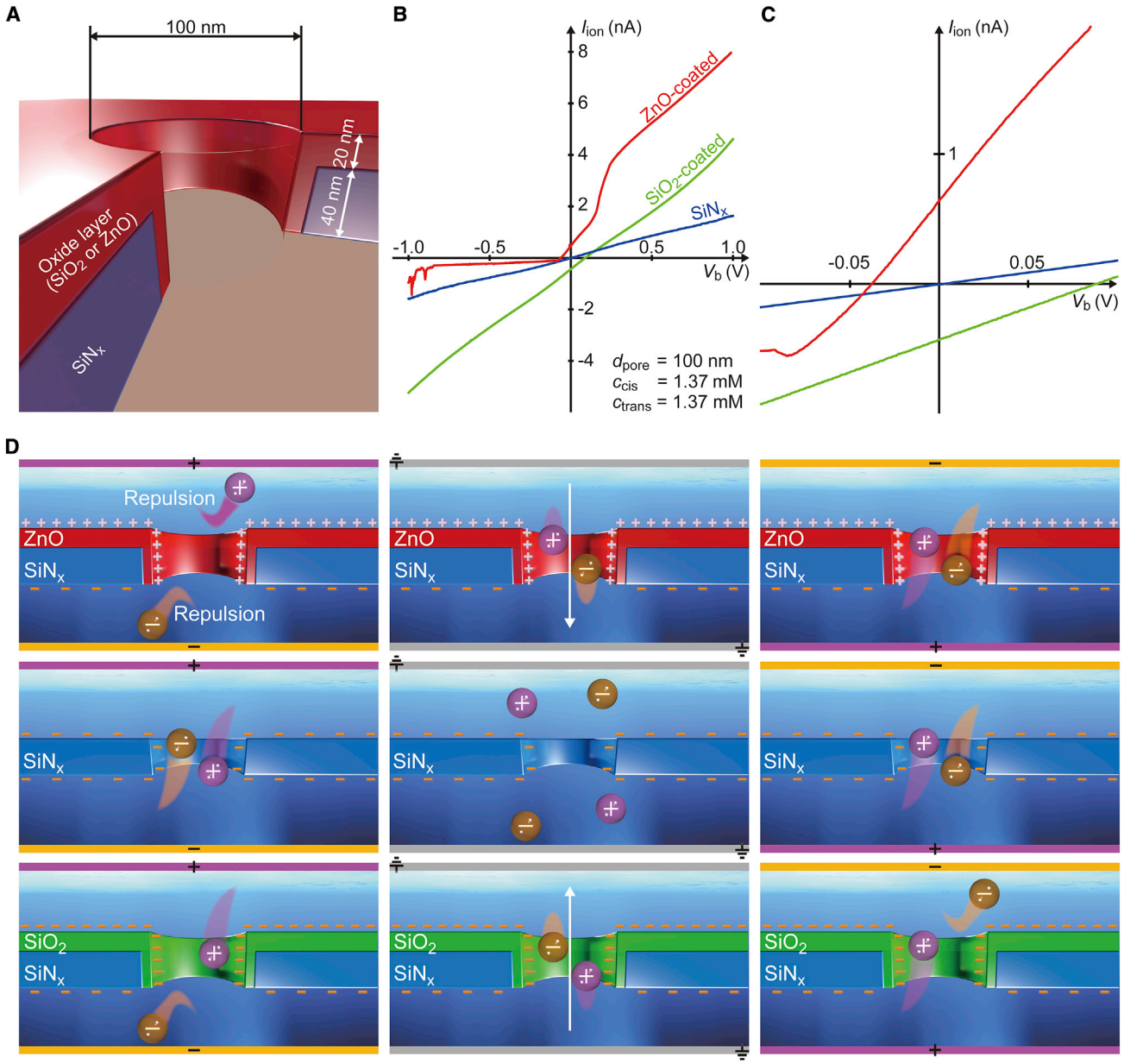

Figure 2. Asymmetric ion transport in one-side coated nanopores

(A) A schematic model of metal oxide-covered SiN_x nanopore membrane.

(B and C) $I_{ion} - V_b$ characteristics (B) and a close-up view at around zero voltage (C) of a 100 nm nanopore with 20 nm-thick ZnO (red) and SiO_2 (blue) coated on the membranes. A result of the SiN_x pore is also shown (green). The salt concentrations at the *cis* and *trans* compartments are 1.37 mM.

(D) Conceptual modes of ion transport in the ZnO (top), SiN_x (middle), and SiO_2 nanopores (bottom) under the applied positive (left), zero (center), and negative transmembrane voltages (right).

electrolyte buffer with no salinity gradients (Figure 2C; no such offsets were present under a high ionic strength condition [c_{cis}, c_{trans} = 1.37 M] irrespective of the coating materials). This can be interpreted as a consequence of the surface charge-mediated cross-membrane electric field in the *cis*-to-*trans* (*trans*-to-*cis*) directions for the ZnO-coated (SiO_2-coated) nanopores driving spontaneous ion flows under zero V_b when the screening by the electrolytes is less effective (Figure 2D). These observations consistently indicate the highly selective nature of the ion transport in the short

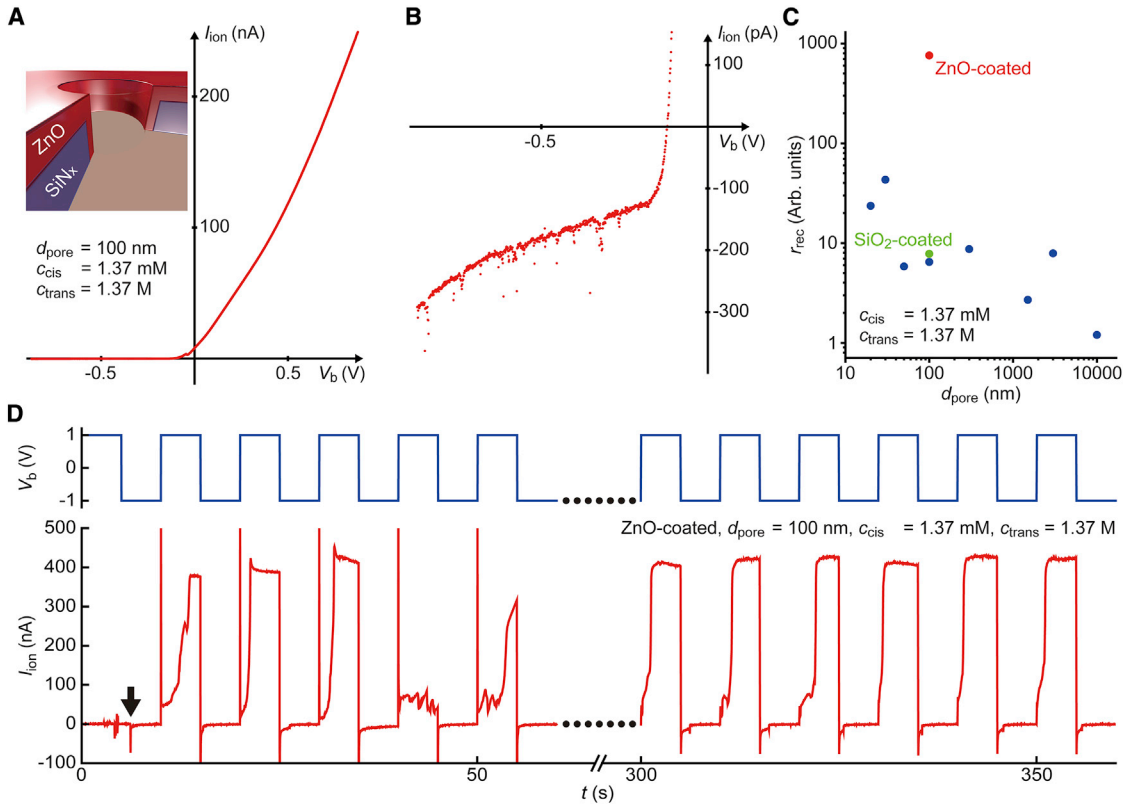

Figure 3. Metal oxide-coated nanopore diodes

(A) Strong rectification of ionic current through a 100 nm-sized ZnO-coated nanopore with the rectification ratio r_{rec} of 833 under r_{ion} = 0.001.

(B) A magnified view of (A).

(C) Pore-size dependence of the rectifying behaviors of SiN_x pores (blue). R_{rec} of the 100 nm-sized ZnO- (red) and SiO_2-coated nanopores (green) is also shown.

(D) Voltage-controlled switching of the ionic conductance of the ZnO nanopore diode under the 1,000-fold salinity difference at the *cis* and *trans*. The temporal response of the I_{ion} against the square wave transmembrane voltage (blue) is shown by the red line. The black arrow indicates the point of time when the voltage is added to the membrane.

nanochannels with little overlap of the electric double layer along with its tunability via the membrane surface functionalization.

The single ZnO/SiN_x nanopores also exhibited strong rectifying behaviors under salinity gradients.[32,33] In contrast to the steep rise in I_{ion} to over 200 nA under a positive voltage sweep to around +1 V (Figure 3A), the current remained at an extremely low level around 200 pA under negative V_b (Figure 3B). The rectification ratio reached above 800, which is about two orders of magnitude higher than that in the SiN_x nanopore (Figure 3C). Moreover, the bimodal states can be switched repeatedly by a cross-membrane voltage control via the slow response of the nanopore conductance (taking several seconds for each transition upon changing V_b between −1 and +1 V), reflecting the relatively stable nature of the ion-depleted/enriched configurations (Figure 3D; see also Figures S13 and S14).

Osmotic energy conversion efficiencies of multi-nanopore membranes

Now, we evaluate the energy conversion efficiency in the short fluidic channels. We extracted V_{dif} and the short circuit current I_{short} from the $I_{ion} - V_b$ characteristics measured under a 1,000-fold difference in the salt concentrations at *cis* and *trans* (Figure 4A).[12] Both V_{dif} and I_{short} are small in the SiN_x micropores of $d_{pore} \geq$

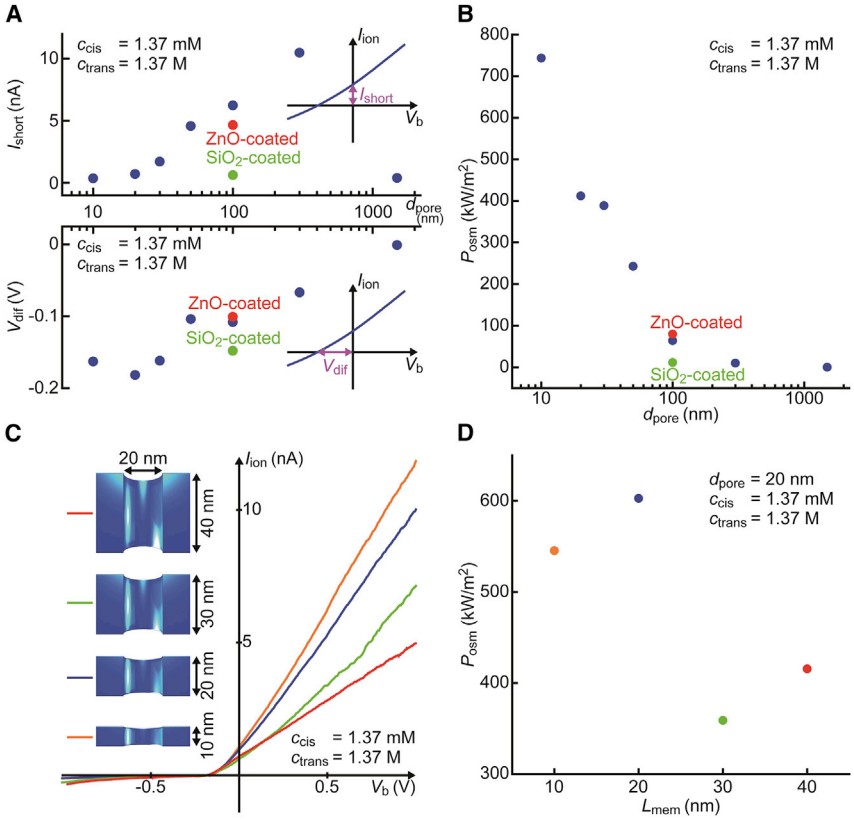

Figure 4. Osmotic power generation with single nanopores

(A) The short-circuit current I_{short} and the diffusion-induced voltage V_{dif} of single SiN_x pores (blue). The results of ZnO- (red) and SiO_2-coated pores (green) are also displayed. Insets explain the definitions of I_{short} and V_{dif}.

(B) The osmotic power per pore area P_{osm} plotted as a function of d_{pore}. Color code is the same as that in (A).

(C) 1,000-fold salinity-gradient-mediated $I_{ion} - V_b$ characteristics of single nanopores of diameter 20 nm in SiN_x membranes of various thickness L_{mem}: L_{mem} = 40 (red), 30 (green), 20 (blue), and 10 nm (orange).

(D) P_{osm} of the 20 nm nanopores plotted as a function of L_{mem}. Color coding is the same as that in (C).

1.5 μm due to the weak ion selectivity in the large channels. Smaller pores, on the other hand, revealed the pronounced cation selectivity as a monotonic increase in $|V_{dif}|$ with decreasing d_{pore}, together with the depressed I_{short} due to the smaller space for the ion transport. As a result, the osmotic power per channel area[14] P_{osm} (= $I_{short}V_{dif}/A_{pore}$, where $A_{pore} = \pi d_{pore}^2/4$ is the nanopore area) demonstrated a sharp rise as the channel size is reduced to below 300 nm and finally reaching over 700 kW/m^2 with the 10 nm-sized nanopore (Figure 4B).

The aspect ratio structure of the 20 nm SiN_x nanopore was further altered by reducing the membrane thickness L_{mem} through dry etching.[34] Thinner L_{mem} led to larger I_{ion} due to the associated decrease in the resistance inside the pore (Figure 4C).[18–20] Meanwhile, V_{dif} remained almost unchanged, suggesting the retained quasi-perfect cation-selective transport in the shallow nanopores. Consequently, P_{osm} is enhanced by a factor of 1.5 to around 600 kW/m^2, which is comparable to the giant energy density reported for the MoS_2 nanopore osmotic power generators (Figure 4D).[12]

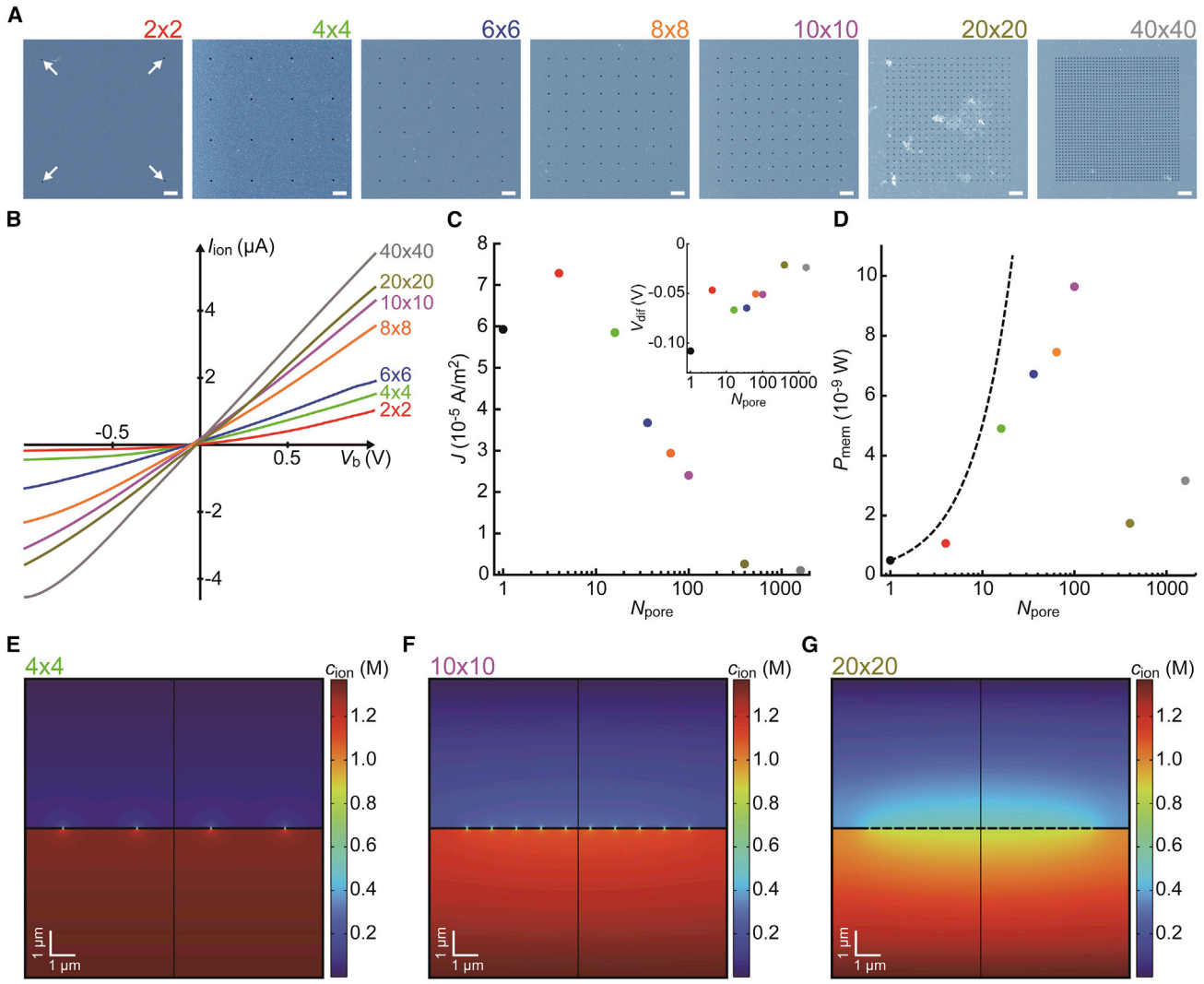

Figure 5. Multi-nanopore membrane osmotic power generators

(A) Scanning electron micrographs of 100 nm-sized multi-nanopores drilled in SiN_x membranes. Scale bars denote 1 μm. The number of pores N_{pore} increases as 4, 16, 36, 64, 100, 400, and 1,600 from the left to right. White arrows are a guide to the eye for the positions of the nanopores.

(B) I_{ion} – V_b characteristics of the 100 nm-sized multi-nanopores. Color coding is the same as that in (C).

(C) The ionic current density J in multi-pores. Inset is V_{dif} plotted against the number of pores N_{pore}.

(D) The osmotic power density per membrane area, P_{mem}, plotted with respect to N_{pore} in a 10 μm-square area.

(E–G) Finite element calculations of the ion concentration profiles around the multi-nanopores of N_{pore} = 16 (E), 100 (F), and 400 (G).

While demonstrating the efficient power generation capability of the single solid-state nanopores, its practical feasibility needs further verifications by characterizing the ion transport properties in a bulk form.[14,15] For this, we delineated various 2D patterns of 100 nm nanopores in the 100 μm-square area of a SiN_x membrane by electron beam lithography to assess the ion permeability of multi-pore membranes (Figure 5A). I_{ion} – V_b curves tended to be steeper as we increased the number of pores N_{pore} from 4 to 1,600 due to the larger gross ion flow through the membrane of higher porosity (Figure 5B). At the same time, the rectifying behavior became weaker, suggestive of mitigated salt concentration gradients at the densely packed nanopores (Figure S15).[15] As a consequence, V_{dif} tended to become lower with N_{pore}. Moreover, the current density J, which is calculated as $J = I_{short}/A_{multi}$ with the total area of the multi-pores A_{multi}, was found to decrease with increasing the porosity.

Broadened salt concentration distributions via inter-pore interference

To shed light on these intriguing features, we performed finite element simulations of the ion diffusion in the salinity gradient-biased multi-nanopores (Figure S16). In the case of N_{pore} less than 16, i.e., an inter-pore distance d_{int} longer than 3 μm, the salinity gradients were observed only at the vicinities of the nanopores (Figure 5E). In contrast, shorter d_{int} induced significant spatial broadening of the ion concentration distributions due to the overlaps of the diffusion layers among the multi-channels (Figures 5F and 5G).[35,36] This significant inter-pore interference explains the diminished diffusive ion flux across the closely spaced multi-pore membrane.

The overall N_{pore} dependence of the ionic current characteristics led to a diminished osmotic power density, P_{mem}, in the 10 μm area than that expected from the performance of the single nanopore (dashed curve in Figure 5C). Yet, it still demonstrates an optimal osmotic power generation capability of 100 W/m^2 at 1% porosity with 1 μm grid spacing (Figure 5C). This power density is to be compared with the performances of the other nanofluidic power generators, where the state-of-the-art functional membranes were demonstrated to gain energy density of several tens of W/m^2.[35–38] The sparse multi-nanopores can thus be regarded as an efficient osmotic energy convertor.

DISCUSSION

The present work experimentally proved the crucial importance of not only the ion selectivity of individual channels but their density in a membrane to gain large osmotic power outputs. Future efforts should thus be directed to find fabrication procedures that can control the number and positions of nanochannels in the functional membranes already known as high-performance osmotic power generators.[12,37–40] For the synthetic ultrathin membranes, in particular, there are additional issues that need to be addressed such as the anti-fouling characteristics[41,42] and the long-term chemical stability,[43] where one would have to compromise the power and efficiency to meet the requirements for their implementation in a natural environment.

EXPERIMENTAL PROCEDURES

Resource availability

Lead contact

Further information and requests for resources should be directed to and will be fulfilled by the lead contact, Makusu Tsutsui (tsutsui@sanken.osaka-u.ac.jp).

Materials availability

This study did not generate new unique reagents.

Data and code availability

- All data reported in this paper will be shared by the lead contact upon request.
- This paper does not report original code.
- Any additional information required to reanalyze the data reported in this paper is available from the lead contact upon request.

Fabrication of micro- and nanopores

A 4 inch silicon wafer, whose both sides were covered with 50 nm-thick SiN_x layers by low-pressure chemical vapor deposition, was cut into 30 × 30 mm chips. One side of the SiN_x was partially removed by reactive ion etching (RIE-10NR, Samco) in the CHF_3 atmosphere through a metal mask having a 1 × 1 mm window. The chip was then immersed in KOH aqueous solution (Aldrich) and heated at 80°C. The silicon

layer was dissolved by this wet-etching process, creating a deep trench with a 40 nm-thick SiN_x membrane at the bottom. Subsequently, micro- or nanometer-scale holes were formed in the membrane. For this, a resist layer (ZEP520A) was spin coated on the membrane. Prebaking at 180°C on a hot plate, circles of diameter d_{pore} were delineated by an electron beam lithography (Elionix). After development, a hole of diameter d_{pore} was sculpted by dry etching the SiN_x by the reactive ion etching using the residual resist layer as a mask. Finally, the chip was cleaned by immersing it in *N*,*N*-dimethylformamide overnight, followed by rinsing with ethanol and acetone.

Dielectric coating

A nanopore of d_{pore} = 120 nm was created in a 40 nm-thick SiN_x membrane by the procedure described above. We deposited a ZnO or SiO_2 layer of thickness 20 nm on the nanopore membrane by a radio-frequency magnetron sputtering. After this, the nanopore shrunk to approximately 100 nm in diameter, which suggests coating of not only the membrane but also the nanopore wall surface by the dielectric layer.

Ionic current measurements

A nanopore chip was sealed with two blocks made of polydimethylsiloxane (PDMS). The polymer blocks were prepared by curing of a PDMS precursor (Sylgard184, Dow) on an SU-8 mold. Each block had an I-shaped trench at one side of the surface, which served as a fluidic channel to flow electrolyte solution into the pores. Before sealing the chip, three holes were punched into each of the two blocks. A nanopore chip and two PDMS blocks were then treated with oxygen plasma for surface activation. Subsequently, the blocks were adhered to on both sides of the chip. After that, the pore was filled with electrolyte buffer by flowing it through one of the three holes in each PDMS block. Inserting two Ag/AgCl rods into another hole in the polymeric block, the cross-membrane ionic current I_{ion} was measured under the applied voltage V_b using a picoammeter/voltage source unit (Keithley6487, Keithley). When scanning voltage, V_b was changed at 5 mV step taking about 100 s to complete one voltage sweep from −1 to 1 V.

Finite element simulations

The distributions of ions around multi-pore membranes were numerically simulated by simultaneously solving the Poisson-Boltzmann equation for electric potential and the Nernst-Planck equation for ion concentration.[36] The electrostatic potential (V) was given by

$$\nabla^2 V = -\frac{1}{\varepsilon_w} F \sum_i z_i c_i \exp(-z_i e V / k_B T), \qquad \text{(Equation 1)}$$

where ε_w, F, e, k_B, and T were the permittivity of water (7.08×10^{-10} F/m), the Faraday constant (96,500 C/mol), the elementary charge (1.60×10^{-19} C), the Boltzmann constant (1.38×10^{-23} J/K), and the temperature (293 K), respectively. c_i and z_i were the concentrations and valence of Na^+ and Cl^- for i ion (z_i = 1 for i = Na^+ and z_i = −1 for i = Cl^-). The ion concentration was calculated by

$$\nabla \cdot (-D_i \nabla c_i - z_i u_i F c_i \nabla V) = 0. \qquad \text{(Equation 2)}$$

Here, u_i is the electrical mobility for i ion ($u_i = 5.28 \times 10^{-8}$ m^2/V·s for i = Na^+ and $u_i = 8.04 \times 10^{-8}$ m^2/V·s for i = Cl^-), and the diffusion coefficient was evaluated as $D_i = u_i k_B T/e$. The multi-pore structures were modeled in a 3D Cartesian coordinates system with mirror symmetry (Figure S16). The model size was 12 μm in width and 12 μm in depth in x and y directions (from 0 to 12 μm) and 24 μm in height in the z direction

(from −12 to 12 μm). The 40 nm-thickness membrane was positioned at z = 0 μm (−20 to 20 nm), in which the array of 50 nm-radius pores was formed at an interval of $9/(N_{pore}{}^{0.5} - 1)$ μm. On the membrane and pore surfaces, a surface charge of −10 mC/m^2 was set, and ground at z = 12 μm and a bias voltage of 0 V at z = −12 μm were the boundary conditions for solving Equation 1. As the boundary conditions for Equation 2, c_i = 1.37 mM (z = −24 μm), 1.37 M (z = 24 μm), and symmetry (x = 0 μm and y = 0 μm) were employed. All the calculations were performed by COMSOL Multiphysics 6.0 (COMSOL, Stockholm, Sweden).

SUPPLEMENTAL INFORMATION

Supplemental information can be found online at https://doi.org/10.1016/j.xcrp.2022.101065.

ACKNOWLEDGMENTS

A part of this work was supported by the Japan Society for the Promotion of Science (JSPS) KAKENHI grant numbers 22H01926 and 22K04893.

AUTHOR CONTRIBUTIONS

Conceptualization, M.T. and T.K.; methodology, M.T. and K.Y.; investigation, M.T., K.Y., and Y.H.; writing – original draft, M.T. and K.T.; writing – review & editing, M.T. and T.K.; funding acquisition, M.T. and K.Y.; resources, M.T. and K.Y.; supervision, T.K.

DECLARATION OF INTERESTS

The authors declare no competing interests.

Received: June 1, 2022
Revised: July 21, 2022
Accepted: August 30, 2022
Published: October 7, 2022

REFERENCES

1. Guo, W., Cao, L., Xia, J., Nie, F.-Q., Ma, W., Xue, J., Song, Y., Zhu, D., Wang, Y., and Jiang, L. (2018). Energy harvesting with single-ion-selective nanopores: a concentration-gradient-driven nanofluidic power source. Adv. Funct. Mater. *20*, 1339–1344.

2. Thomas, M., Corry, B., and Hilder, T.A. (2014). What have we learnt about the mechanisms of rapid water transport, ion rejection, and selectivity in nanopores from molecular simulation? Small *10*, 1453–1465.

3. Zhang, Z., Wen, L., and Jiang, L. (2021). Nanofluidics for osmotic energy conversion. Nat. Rev. Mater. *6*, 622–639.

4. Rahman, A., Farrok, O., and Haque, M.M. (2022). Environmental impact of renewable energy source based electrical power plants: solar, wind, hydroelectric, biomass, geothermal, tidal, ocean, and osmotic. Renew. Sustain. Energy Rev. *161*, 112279.

5. Vlassiouk, I., Smirnov, S., and Siwy, Z. (2008). Ion selectivity of single nanochannels. Nano Lett. *8*, 1978–1985.

6. Zhang, Z., He, L., Zhu, C., Qian, Y., Wen, L., and Jiang, L. (2020). Improved osmotic energy conversion in heterogeneous membrane boosted by three-dimensional hydrogel interface. Nat. Commun. *11*, 875.

7. Liu, Y.-C., Yeh, L., Zheng, M.-J., and Wu, K.C.W. (2021). Highly selective and high-performance osmotic power generators in subnanochannel membranes enabled by metal-organic frameworks. Sci. Adv. *7*, abe9924.

8. Bao, B., Hao, J., Bian, X., Zhu, X., Xiao, K., Liao, J., Zhou, J., Zhou, Y., and Jiang, L. (2017). 3D porous hydrogel/conducting polymer heterogeneous membranes with electro-/pH-modulated ionic rectification. Adv. Mater. *29*, 1702926.

9. Chen, W., Wang, Q., Chen, J., Zhang, Q., Zhao, X., Qian, Y., Zhu, C., Yang, L., Zhao, Y., Kong, X.Y., et al. (2020). Improved ion transport and high energy conversion through hydrogel membrane with 3D interconnected nanopores. Nano Lett. *20*, 5705–5713.

10. Laucirica, G., Albesa, A.G., Toimil-Molares, M.E., Trautmann, C., Marmisollé, W.A., and Azzaroni, O. (2020). Shape matters: enhanced osmotic energy harvesting in bullet-shaped nanochannels. Nano Energy *71*, 104612.

11. Rollings, R.C., Kuan, A.T., and Golovchenko, J.A. (2016). Ion selectivity of graphene nanopores. Nat. Commun. *7*, 11408.

12. Feng, J., Graf, M., Liu, K., Ovchinnikov, D., Dumcenco, D., Heiranian, M., Nandigana, V., Aluru, N.R., Kis, A., and Radenovic, A. (2016). Single-layer MoS_2 nanopores as nanopower generators. Nature *536*, 197–200.

13. Macha, M., Marion, S., Nandigana, V.V.R., and Radenovic, A. (2019). 2D materials as an emerging platform for nanopore-based power generation. Nat. Rev. Mater. *4*, 588–605.

14. Cao, L., Wen, Q., Feng, Y., Ji, D., Li, H., Li, N., Jiang, L., and Guo, W. (2018). On the origin of ion selectivity in ultrathin nanopores: insights for membrane-scale osmotic energy conversion. Adv. Funct. Mater. *28*, 1804189.

15. Wang, L., Wang, Z., Patel, S.K., Lin, S., and Elimelech, M. (2021). Nanopore-based power generation from salinity gradient: why it is not viable. ACS Nano *15*, 4093–4107.

16. Gadaleta, A., Sempere, C., Gravelle, S., Siria, A., Fulcrand, R., Ybert, C., and Bocquet, L. (2014). Sub-additive ionic transport across

arrays of solid-state nanopores. Phys. Fluid *26*, 012005.

17. Tsutsui, M., Arima, A., Yokota, K., Baba, Y., and Kawai, T. (2022). Ionic heat dissipation in solid-state pores. Sci. Adv. *8*, eabl7002.

18. Garaj, S., Hubbard, W., Reina, A., Kong, J., Branton, D., and Golovchenko, J.A. (2010). Graphene as a subnanometre trans-electrode membrane. Nature *467*, 190–193.

19. Tsutsui, M., Hongo, S., He, Y., Taniguchi, M., Gemma, N., and Kawai, T. (2012). Single-nanoparticle detection using a low-aspect-ratio pore. ACS Nano *6*, 3499–3505.

20. Sahu, S., and Zwolak, M. (2018). Maxwell-Hall access resistance in graphene nanopores. Phys. Chem. Chem. Phys. *20*, 4646–4651.

21. Arjmandi, N., van Roy, W., Lagae, L., and Borghs, G. (2012). Measuring the electric charge and zeta potential of nanometer-sized objects using pyramidal-shaped nanopores. Anal. Chem. *84*, 8490–8496.

22. van Dorp, S., Keyser, U.F., Dekker, N.H., Dekker, C., and Lemay, S.G. (2009). Origin of the electrophoretic force on DNA in solid-state nanopores. Nat. Phys. *5*, 347–351.

23. Zhang, S., Yang, L., Ding, D., Gao, P., Xia, F., and Bruening, M.L. (2021). Highly rectifying fluidic diodes based on asymmetric layer-by-layer nanofilms on nanochannel membranes. Anal. Chem. *93*, 4291–4298.

24. Graf, M., Lihter, M., Unuchek, D., Sarathy, A., Leburton, J.P., Kis, A., and Radenovic, A. (2019). Light-enhanced blue energy generation using MoS_2 nanopores. Joule *3*, 1549–1564.

25. Kim, D.K., Duan, C., Chen, Y.F., and Majumdar, A. (2010). Power generation from concentration gradient by reverse electrodialysis in ion-selective nanochannels. Microfluid. Nanofluidics *9*, 1215–1224.

26. Bard, A.J., and Faulkner, L.R. (2001). Electrochemical Methods (John Wiley & Sons, Inc.).

27. Ma, L., An, X., Song, F., and Qiu, Y. (2022). Effective charged exterior surfaces for enhanced ionic diffusion through nanopores under salt gradients. J. Phys. Chem. Lett. *13*, 5669–5676.

28. Eggenberger, O.M., Ying, C., and Mayer, M. (2019). Surface coatings for solid-state nanopores. Nanoscale *11*, 19636–19657.

29. Wood, M., and Zhang, B. (2015). Bipolar electrochemical method for dynamic in situ control of single metal nanowire growth. ACS Nano *9*, 2454–2464.

30. Yang, H.C., Xie, Y., Hou, J., Cheetham, A.K., Chen, V., and Darling, S.B. (2018). Janus membranes: creating asymmetry for energy efficiency. Adv. Mater. *30*, 1801495.

31. Beitollahi, H., Tajik, S., Garkani Nejad, F., and Safaei, M. (2020). Recent advances in ZnO nanostructure-based electrochemical sensors and biosensors. J. Mater. Chem. B *8*, 5826–5844.

32. Daiguji, H., Oka, Y., and Shirono, K. (2005). Nanofluidic diode and bipolar transistor. Nano Lett. *5*, 2274–2280.

33. Vlassiouk, I., and Siwy, Z.S. (2007). Nanofluidic diode. Nano Lett. *7*, 552–556.

34. Wanunu, M., Dadosh, T., Ray, V., Jin, J., McReynolds, L., and Drndić, M. (2010). Rapid electronic detection of probe-specific microRNAs using thin nanopore sensors. Nat. Nanotechnol. *5*, 807–814.

35. Amatore, C., Oleinick, A.I., and Svir, I. (2009). Theory of ion transport in electrochemically switchable nanoporous metallized membranes. ChemPhysChem *10*, 211–221.

36. Yang, J., Tu, B., Zhang, G., Liu, P., Hu, K., Wang, J., Yan, Z., Huang, Z., Fang, M., Hou, J., et al. (2022). Advancing osmotic power generation by covalent organic framework monolayer. Nat. Nanotechnol. *17*, 622–628.

37. Wan, J., Huang, L., Wu, J., Xiong, L., Hu, Z., Yu, H., Li, T., and Zhou, J. (2018). Microwave combustion for rapidly synthesizing pore-size-controllable porous graphene. Adv. Funct. Mater. *28*, 1800382.

38. Chen, J., Xin, W., Chen, W., Zhao, X., Qian, Y., Kong, X.Y., Jiang, L., and Wen, L. (2021). Biomimetic nanocomposite membranes with ultrahigh ion selectivity for osmotic power conversion. ACS Cent. Sci. *7*, 1486–1492.

39. Zhang, Z., Yang, S., Zhang, P., Zhang, J., Chen, G., and Feng, X. (2019). Mechanically strong Mxene/Kevlar nanofiber composite membranes as high-performance nanofluidic osmotic power generators. Nat. Commun. *10*, 2920.

40. Cao, L., Chen, I.-C., Chen, C., Shinde, D.B., Liu, X., Li, Z., Zhou, Z., Zhang, Y., Han, Y., and Lai, Z. (2022). Giant osmotic energy conversion through vertical-aligned ion-permselective nanochannels in covalent organic framework membranes. J. Am. Chem. Soc. *144*, 12400–12409. https://doi.org/10.1021/jacs.2c04223.

41. Li, X., Cai, T., and Chung, T.S. (2014). Anti-fouling behavior of hyperbranched polyglycerol-grafted poly(ether sulfone) hollow fiber membrane for osmotic power generation. Environ. Sci. Technol. *48*, 9898–9907.

42. Schneider, G.F., Xu, Q., Hage, S., Luik, S., Spoor, J.N.H., Malladi, S., Zandbergen, H., and Dekker, C. (2013). Tailoring the hydrophobicity of graphene for its use as nanopores for DNA translocation. Nat. Commun. *4*, 2619.

43. Chou, Y.C., Masih Das, P., Monos, D.S., and Drndić, M. (2020). Lifetime and stability of silicon nitride nanopores and nanopore arrays for ionic measurements. ACS Nano *14*, 6715–6728.